communications materials

A Nature Portfolio journal

Article

https://doi.org/10.1038/s43246-026-01411-7

Chemically and microstructurally modulated high-temperature release of CsI in Nd-doped UO_2 nanoceramics

Check for updates

Daniil Shirokiy[1] ✉, Karin Popa[2] ✉, Marco Cologna[2], Felix Brandt[1], Jean-Yves Colle[2], Damien Prieur[3,4], Olaf Walter[2], Walter Bonani[2], Anna Isabel Martinez Ferri[2], Ondřej Beneš[2], Martina Klinkenberg[1], Răzvan Buda[2], Dirk Bosbach[1] & Gabriel L. Murphy[1] ✉

The unexpected discharge of instant release fraction elements, such as Cs and I, from irradiated nuclear fuel, is one of the most concerning severe events that may occur during in-pile irradiation, the subsequent storage and final disposal, yet the underlying chemistry behind their release is poorly understood. Herein, we have examined the speciation of CsI within UO_2 nanoceramics doped with Nd as a proxy for high burn-up fuel, which was synthesised via spark plasma sintering. We demonstrate via X-ray absorption spectroscopy and electron microscopy that the addition of Nd has an impact upon the chemical speciation and dissociation of CsI in the examined materials. High temperature release studies using Knudsen effusion mass spectrometry reveal varying release patterns corresponding to Nd addition. The results of this investigation indicate that the chemistry of the UO_2 high burn-up fuel matrix, its specific microstructure and associated soluble fission products impact the chemical speciation and the high temperature release of Cs and I within irradiated fuel.

In the pursuit of reducing the volume of spent nuclear fuel (SNF) and increasing energy production efficiency, there is an increasing demand for more efficient, higher burn-up nuclear fuels[1–4]. Increased fuel burn-up results in a correspondingly higher content of fission products (FPs), whereas when the local burn-up of typical nuclear UO_2 fuel exceeds 55 GWd/tHM, microstructural changes occur, and what is known as the "high burn-up structure" (HBS) emerges[5–7]. The HBS comprises nano-grains measuring ~100–500 nm[7,8], and is characterised by an increased content of FPs and higher porosity, caused by the development of fission gas pores[5,9]. These structures are often observed at the periphery of a SNF pellet, where temperatures are lower while thermal neutron fluxes and accordingly burn-ups are typically higher; hence, they are referred to as "rim structures"[7,10]. The exact mechanism underlying the formation of the HBS is still the subject of debate[11]. Some works suggest that it may result from the emergence and growth of fission gas bubbles, followed by the formation of small sub-grains from the original grains[5,12], or that these processes occur simultaneously[11,13–15]. Interest in the study of the HBS is attracted by its ability to influence the mechanical properties and swelling of fuel, as well as the release of gaseous and volatile FPs during reactor irradiation, or during an unexpected fuel breach event. Specifically, a high concentration of porosity in the restructured fuel region could lead to unsustainable swelling of the fuel, causing mechanical instability during reactivity-initiated accidents[7]. At the same time, the HBS is known to exhibit improved thermal conductivity and fission gas retention, which hinders release[9,11,16,17].

What is known as the instant release fraction (IRF) is considered one of the most concerning radionuclide release processes, as it can readily compromise the integrity and safety of irradiated fuel when in a reactor, in storage, or within a repository. The IRF is defined as the proportion of FPs radionuclides that are not chemically bound in the UO_2 fuel matrix and can be rapidly released from fuel or fuel assemblies in the event of containment breach[8,18], (for example, due to mechanical impact, corrosion or meltdown) or subsequent contact with water[19,20]. Consequently, understanding the role of the HBS in influencing the release of the IRF is critical for both safe usage and final disposal of high burn-up fuels.

The instantaneous release of radionuclides from irradiated nuclear fuel following a breach event is understood to occur through two mechanisms: from the gap (that includes the fuel-cladding gap and fractures), and from grain boundaries, whereas in the case of a melt-down, a matrix diffusion mechanism is also involved[16,18,21,22]. Elements in the IRF include a series of radioisotopes, with particular attention given here to the radioactive isotopes of iodine (I) and caesium (Cs), including

[1]Institute of Fusion Energy and Nuclear Waste Management (IFN-2), Forschungszentrum Jülich GmbH, Jülich, Germany. [2]European Commission, Joint Research Centre (JRC), Karlsruhe, Germany. [3]Rossendorf Beamline (BM20), European Synchrotron Radiation Facility, Grenoble, France. [4]Institute of Resource Ecology, Helmholtz-Zentrum Dresden-Rossendorf, Dresden, Germany. ✉e-mail: d.shirokiy@fz-juelich.de; karin.popa@ec.europa.eu; g.murphy@fz-juelich.de

^{129}I ($T_{1/2} = 1.57 \cdot 10^7$ y), ^{135}Cs ($T_{1/2} = 2.3 \cdot 10^6$ y) and ^{137}Cs ($T_{1/2} = 30.08$ y). Both elements, Cs and I, belong to the volatile and gaseous FPs group, but Cs also classifies as a FP that forms oxide precipitates[18,23–25]. As the IRF-related elements, Cs and I are typically found in both the fuel-cladding gap and grain boundary regions[19]. Despite thermodynamic calculations predicting the favourability of CsI compound formation in reactor conditions[26], CsI has not often been observed in SNF[27,28]. This has been proposed to be in-part due to γ-induced radiolysis[28,29]. The behaviour and release of Cs and I from irradiated fuel has been studied using numerous methods, such as leaching experiments[16,30–32] and high-temperature methods[33], particularly via Knudsen effusion mass spectrometry (KEMS)[34–38]. Experiments focusing on high burn-up SNF showed that the release of IRF-related radionuclides from HBS regions is different compared to the release from the non-HBS regions of SNF, even when considering variations in FPs inventories[16,30,37]. Consequently, the emergent roles of FP content and the structural-chemical nature of the HBS in dictating behaviour and release of IRF-related radionuclides remain unclear.

Precisely investigating effects pertaining to IRF release from the HBS of irradiated fuel is often achieved via model system methods. Such studies focus on individual effects within SNF while excluding their mutual influence and avoiding the challenges associated with the high radioactivity of actual SNF samples[39–43]. However, they often involve the use of high-temperature stages, such as conventional sintering of UO_2, which typically reach temperatures above 1600 °C[39]. Long sintering at such temperatures above the CsI boiling point (1280 °C) will lead to its complete evaporation, which imposes limitations on the study of the behaviour and chemistry of Cs and I species using CsI-doped UO_2 model systems. Moreover, these sintering conditions lead to significant grain growth[44], which hinders the synthesis of ceramics with grain sizes comparable to the HBS. As an alternative to high-temperature sintering, spark plasma sintering (SPS) allows to sinter materials at lower temperatures and for shorter periods of time, thereby avoiding both complete evaporation of CsI and undesirable grain growth. It is therefore better suited to ensure the incorporation of Cs and I into the nanograined structure of sintered UO_2, enabling the subsequent examination of the associated microstructural effects and release mechanisms to be understood relevant to the actual HBS[45,46].

Previous studies of CsI-doped UO_2 model materials, and their comparison against actual SNF using KEMS revealed different Cs and I release temperatures for each group of samples within the measured ranges, as well as different signal shapes[28,35,37,38]. This suggests that the current model system investigations performed do not completely account for all physical or chemical aspects occurring in actual SNF, promoting the need for more encompassing separate effect studies. The retention of Cs and I up to the temperatures of UO_2 matrix evaporation and their release rates may be influenced by factors such as the microstructure of UO_2, oxygen stoichiometry, radiation fields and the presence of FPs. Pertinently, the role of minor actinides and FPs soluble in fuel matrix, such as lanthanides (*Ln*), in the release of Cs and I has not been examined in model material investigations, nor within microstructures that are consistent with the HBS. Although the IRF-related elements including Cs and I are understood to not incorporate within the UO_2 fuel matrix, van der Waals forces between Cs and I species with the UO_2 matrix can be expected to change with incorporation of soluble FPs due to changes in redox chemistry. This includes the aliovalent substitution of U^{4+} with Ln^{3+}, resulting in the oxidation of U^{4+} to U^{5+}[43,47]. Nevertheless, it remains an open question as to whether matrix-soluble FPs, which occur at higher quantities in higher burn-up fuels, play a significant role in the behaviour and release of IRF elements such as Cs and I, consequently necessitating such investigation.

Considering the pertinence of IRF in higher burn-up fuels potentially occurring during accident scenarios at reactor and repository facilities, it is paramount to determine underlying chemical physics, particularly that of the HBS. This study has consequently examined CsI-incorporated UO_2 model nanoceramic materials with varying levels of neodymium (Nd) as a soluble matrix FP proxy in order to bridge the gap between single-effect studies and those of irradiated fuel to identify key factors contributing to Cs and I chemistry and release. This is achieved through a thorough analysis of the chemistry and behaviour of Cs and I in nanostructured UO_2 mimicking the HBS in the presence of FPs soluble in the UO_2 matrix, including their temperature-induced release. In the present work, Nd was used, since it is known to be an inactive surrogate for minor actinides, such as americium, due to similar matching ionic radii[48,49], and is also highly relevant to the HBS since its local concentration increases linearly with fuel burn-up[5]. The study subsequently examined CsI-included and Nd-doped nanostructured UO_2 samples systematically by varying the levels of Nd from 0, 15 to 30 mol%. Although such levels exceed the amount of minor actinides and Nd in HBS itself[5,23,50,51], the method allows one to reliably probe the influence of Nd presence independently from the other factors, as it provides a greater magnitude of effect upon the material's chemical properties. In SNF, the concentrations of Cs and I may vary depending on burn-up and location; for instance, in SNF from a pressurised water reactor with an average pellet burn-up of ~55 GWd/tHM, they are around 0.06 mol% for I and 0.82 mol% for Cs[51–53]. To achieve greater detection resolution when measuring synthesised material, a target concentration of 1–2 mol% of CsI was selected. To incorporate CsI into the UO_2 structure, SPS was used with sintering conditions, determined during SPS optimisation cycles to synthesise a variable mixture of Nd-doped UO_2 nanopowder with controlled amount of CsI powders. The obtained materials were investigated for their microstructural and chemical surface speciation, bulk chemistry and redox in addition to release mechanisms via energy dispersive X-ray (EDX) spectroscopy, X-ray absorption near edge structure (XANES), and KEMS analysis respectively. The results obtained are discussed in the context of the current understanding of the release of IRF-related Cs/I from the HBS of irradiated fuel with a high burn-up, and the influence of structural chemistry and the inventory of FPs.

Results

Spark plasma sintering parameter and synthesis optimisation

SEM analysis of the pre-sintered powders revealed that Nd doping directly affected the size of the nanoparticles produced from hydrothermal decomposition (see Supplementary Information Note 3). Specifically, increasing the amount of added Nd consistently resulted in a reduced particle size. The charge compensation mechanism of Nd^{3+} incorporation into the UO_2 structure involves the oxidation of U^{4+} to the U^{5+} ion[47,54], which has a smaller ionic radius[48]. Furthermore, in addition to the difference in grain size, variations in chemical composition also influenced the sintering process. In particular, an increase in the amount of Nd added resulted in a shift of the densification curves to higher temperatures. Subsequently the SPS parameters (temperature, time) had to be optimised to achieve a microstructure comparable to that of the HBS, as well as the inclusion and more homogeneous distribution of CsI. Initial tests were conducted on all samples in an argon atmosphere using the following parameters: heating at a rate of 100 °C/min up to 1200 °C, dwell of 1 min and cooling at a rate of 200 °C/min down to 400 °C, followed by uncontrolled cooling. However, electron microscopy of the subsequently examined samples revealed relatively large grains (>2 μm), so the intended microstructure was not present.

Subsequent optimised SPS conditions for the UO_2–(CsI) synthesis involved the following heating parameters: heating at a rate of 100 °C/min to 800 °C with a 1 min dwell, and then cooling to 400 °C at a rate of 200 °C/min followed by uncontrolled cooling to room temperature. The $(U_{0.85}Nd_{0.15})O_2$–(CsI) sample was sintered with slightly modified parameters: heating at a rate of 100 °C/min to 950 °C with a 5 s dwell, and then cooling to 400 °C at a rate of 200 °C/min followed by uncontrolled cooling to room temperature afterwards. In the sample, sintered at 950 °C for 5 s, tiny CsI particles showed a much more homogeneous distribution throughout the microstructure of the sample, consequently these SPS parameters were selected for sintering of all subsequent samples. The overview of the SPS parameters tested is presented in Table 1. Figure 1 shows the microstructures of the samples sintered at the selected (see Table 1) SPS parameters.

Table 1 | Tested SPS parameters during optimisation cycles

Cycle №	Sintering piston pressure	Heating	Dwell	Cooling
1	70.7 MPa	100 °C/min	1200 °C; 1 min	200 °C/min down to 400 °C, followed by uncontrolled cooling
2			800 °C; 1 min	
3 (selected)			950 °C; 5 s	

The parameters used for cycle No. 3 were selected for synthesising all subsequent samples in the present investigation.

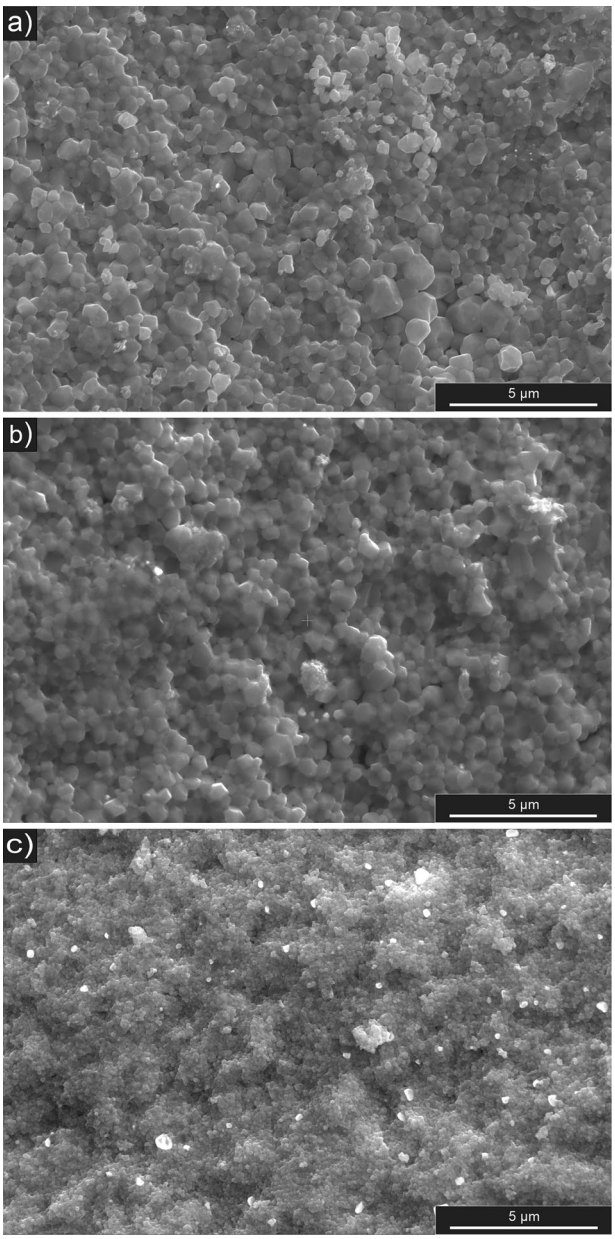


Fig. 1 | Microstructure of pellet cross-section. SEM secondary electron (SE) images showing the microstructure of pellet cross-sections: **a** UO_2–(CsI), **b** $(U_{0.85}Nd_{0.15})O_2$–(CsI), and **c** $(U_{0.7}Nd_{0.3})O_2$–(CsI), sintered using the SPS parameters selected in the Cycle 3 provided in Table 1. The bright white spots correspond to CsI particles.

Via image analysis of the collected SEM micrographs, the average grain size of the synthesised nanoceramics was determined. It was found that grain sizes of 557 ± 133 nm for UO_2–(CsI), 402 ± 63 nm $(U_{0.85}Nd_{0.15})O_2$–(CsI) and 133 ± 17 nm $(U_{0.7}Nd_{0.3})O_2$–(CsI) were ascertained. These results show a trend towards decreased grain size with increased Nd content consistent with the observations of the precursor material (Supplementary Information Note 2).

Attempts were made to determine the density of the synthesised samples using the Archimedes' method, where high density values consistent with previous studies of SPS synthesised UO_2 nanomaterials[55]. However, repeat measurements revealed variations in the determined values, which although were high and consistent with previous investigations[55], could not be reported. Nevertheless, observation of the SEM-SE images of Fig. 1 reveals microstructures devoid of open, connected or isolated porosity that are entirely consistent with high density UO_2 nanoceramics prepared via SPS synthesis[55].

Analysis of the sintered materials using ICP-MS showed that the concentrations of U and Nd corresponded to the targeted synthesis additions within the limits of the ICP-MS measurement error. The Cs concentration was found to be between 0.9–2.1 mol%, although it should be noted that, despite the selected sintering parameters enabled a more homogeneous distribution of CsI particles to be achieved, their concentration within the sample still varied. It was not possible to directly measure I from ICP-MS, however in considering previous work[45] performed on the synthesis of pure UO_2 with CsI included via SPS, additions of I were found systematically corresponding Cs mol %. Nevertheless, the use of Nd may add inconsistencies, to this and as this is the first such study involving the Nd addition with Cs/I simultaneously, variations in the final Cs:I ratio may be possible. The Table 2 lists the compositions of the samples.

X-ray diffraction and material characterisation

To determine the phase purity of the synthesised materials, XRD measurements at room temperature were performed and revealed that synthesised CsI-included Nd-doped UO_2 materials adopted single-phase structures consistent with fluorite UO_2. No secondary phases arising from, for instance, non-lattice incorporated Nd, CsI or Cs and I species could be resolved. The formation of a single-phase solid solution is consistent with previous studies considering the Nd doping levels[54]. The diffractograms as well as the Rietveld refinement profiles in the 2θ ranges of 20–70° are provided in Fig. 2. Determined lattice parameters, as provided in Fig. 2, indicate that the samples are partially oxidised beyond stoichiometric values and would be best regarded as $(U_{1-y}Nd_y)O_{2+x}$–(CsI). This occurred because the sintering time of 5 s was too short to achieve a higher degree of stoichiometry in the O/M ratio[56]. To determine the oxygen excess in the samples, Eq. (1) from the literature[57], which focuses on calculating the $(U_{1-y}Nd_y)O_{2+x}$ lattice parameter, was used.

$$a = \frac{4}{\sqrt{3}}\left\{(1-2y-2x)r_{U^{4+}} + (y+2x)r_{U^{5+}} + yr_{Nd^{3+}} + \frac{(2+x)}{2}r_{O^{2-}} - \frac{x}{2}r_{O^{V}}\right\} \times \left(1-\frac{y}{200}\right) \quad (1)$$

with a – lattice parameter, y – Nd concentration from the ICP-MS measurements, x – oxygen excess, r – ionic radii[48,58]. Based on the calculations following x values in $(U_{1-y}Nd_y)O_{2+x}$ were determined: for the sample UO_2–(CsI) – 0.069(22); for the sample $(U_{0.85}Nd_{0.15})O_2$–(CsI) – 0.100(33) and for the sample $(U_{0.7}Nd_{0.3})O_2$–(CsI) – 0.047(22).

Table 2 | ICP-MS analysis results for quantitative determination of U, Nd and Cs present with investigated samples

Sample	U, mol%	Nd, mol%	Cs, mol%
UO_2–(CsI)	100.00 ± 0.42	0.00 ± 0.42	0.936 ± 0.005
$(U_{0.85}Nd_{0.15})O_2$–(CsI)	85.62 ± 3.47	14.38 ± 3.47	1.400 ± 0.049
$(U_{0.7}Nd_{0.3})O_2$–(CsI)	65.36 ± 8.24	34.64 ± 8.24	2.069 ± 0.171

Thus, based on ICP-MS analysis and oxygen stoichiometry calculations, the final chemical formulas for the samples are as follows: $UO_{2.069}(CsI)_{0.009}$, $(U_{0.856}Nd_{0.144})O_{2.1}(CsI)_{0.014}$ and $(U_{0.654}Nd_{0.346})O_{2.047}(CsI)_{0.021}$, which for simplicity referred as Nd 0%, Nd 15% and Nd 30% respectively later in the text.

To verify the structural stability of the samples and confirm the consistency of their phase composition at high temperature, particularly as to whether they are stable and do not undergo temperature-induced decomposition in vacuum or other phenomena that may impact subsequent KEMS investigations (described in following sections), VT-XRD measurements were performed under vacuum conditions in range of 30–1150 °C. The diffractograms for all measured compositions are provided in Fig. 3.

Inspecting Fig. 3, no additional or vanished peaks are observed in all diffractograms up to 1150 °C under vacuum indicating that there is no loss of Nd or formation of secondary phases. The temperature dependence of the lattice parameters, as determined by Rietveld analysis illustrated in Fig. 4, reveals a linear relationship as a function of temperature, which further indicates that there have been no changes to the structural chemistry of the investigated samples. For UO_2, changes in the linear expansion of the lattice parameter with temperature can indicate partial reduction or oxidation. For instance, under vacuum conditions, reduction and decomposition can occur which would be indicated by a loss of the linear trend in lattice parameter thermal expansion. The observation of a linear trend in Fig. 4 over the prescribed temperature range, indicates structural stability at higher temperatures and maintenance of the UO_2 structure without reduction or decomposition.

Spectroscopic investigations of Cs and I speciation

To explore potential Nd-induced speciation of CsI away from its original state, EDX spectroscopy mapping was performed at different locations on the surface of the ceramic samples' cross-sections, two per sample. The regions were selected following a procedure whereby: 1 – at a location where a relatively large CsI particle (or several) was observed, and 2 – at a location where multiple fine CsI particles were observed. Maps were taken of the C K-edge, O K-edge, I L-edge, Cs L-edge, Nd L-edge, and U M-edge. Figure 5 shows the results of EDX mapping with maps of I and Cs compared for the three samples: Nd 0%, Nd 15% and Nd 30% with two different locations for each. The Supplementary Information Note 5 provides the overlaid maps with an associated overview of the pellet cross-section indicating the mapping relative locations.

EDX mapping results showed that in the case of the Nd-free Nd 0% sample, the distribution of I and Cs always coincided, indicating that these elements remained in the form of CsI particles. Contrastingly, in the Nd 15% sample, mutually exclusive regions consisting of heightened amounts of Cs were observed. The fact that signals of Cs and I occur at different concentrations across the surface suggests that these elements have speciated beyond stoichiometric CsI states. In the higher Nd-doped Nd 30% sample, this speciation becomes more pronounced, as can be seen from the multiple more intense Cs areas. Furthermore, quantitative EDX spot measurements carried out on the surface of each sample (see Supplementary Information Note 1) also show that the Cs/I ratio increases as the Nd content of the samples rises. EDX maps of Nd, provided in Supplementary Information Note 6 in case of the 30% Nd doped sample, show that the UO_2 matrix has a homogeneous distribution of Nd, whereas regions containing Cs and I phases show both depletion and subtle variation. The use of numerous distinct examined regions in both Nd-doped and non-doped sample measurements, does strongly suggest variability in the speciation of CsI as Nd is introduced into the samples.

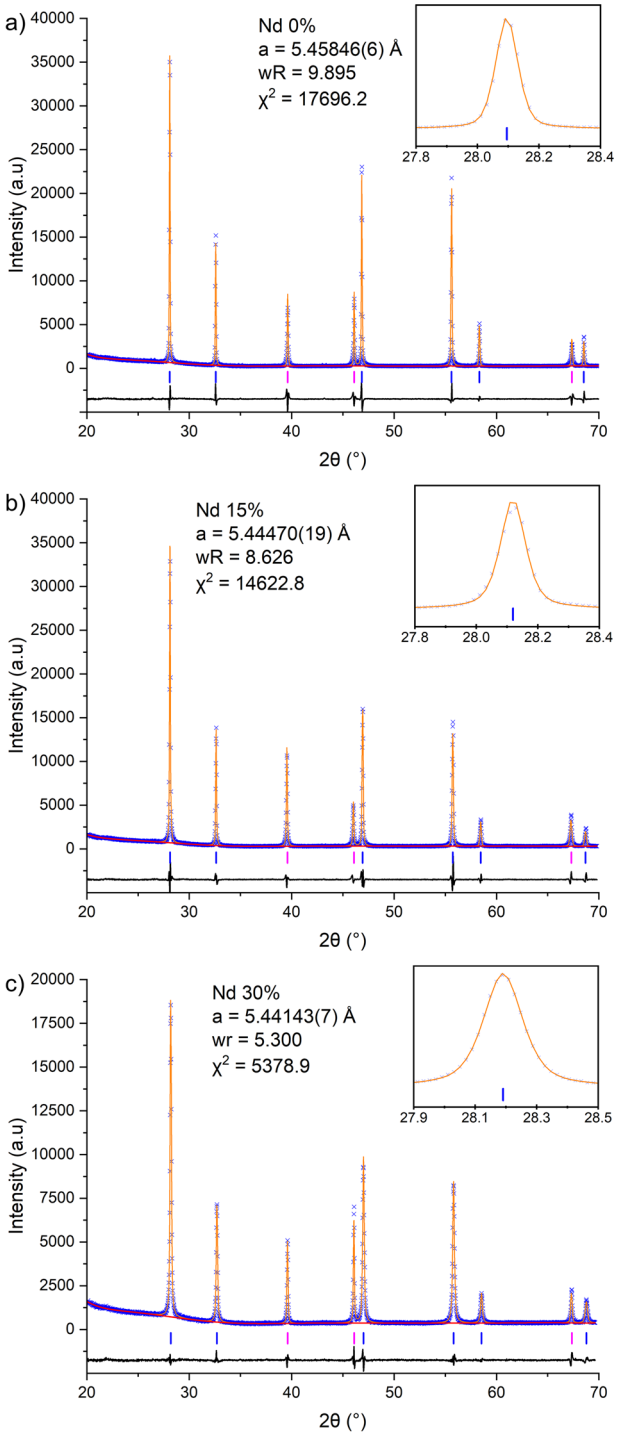


Fig. 2 | Rietveld refinement profiles of synthesised materials. Room temperature XRD diffractograms (blue) with Rietveld refinement profiles (orange), background (red) and difference curves (black) for **a** Nd 0%, **b** Nd 15% and **c** Nd 30% sintered for 5 s at 950 °C in the 2θ range of 20–70°. Allowed reflections of the $Fm\bar{3}m$ space group for fluorite UO_2 and Pt are respectively represented by blue and purple markers. The graph insets show the main peak area crop highlights the single phase nature of the samples.

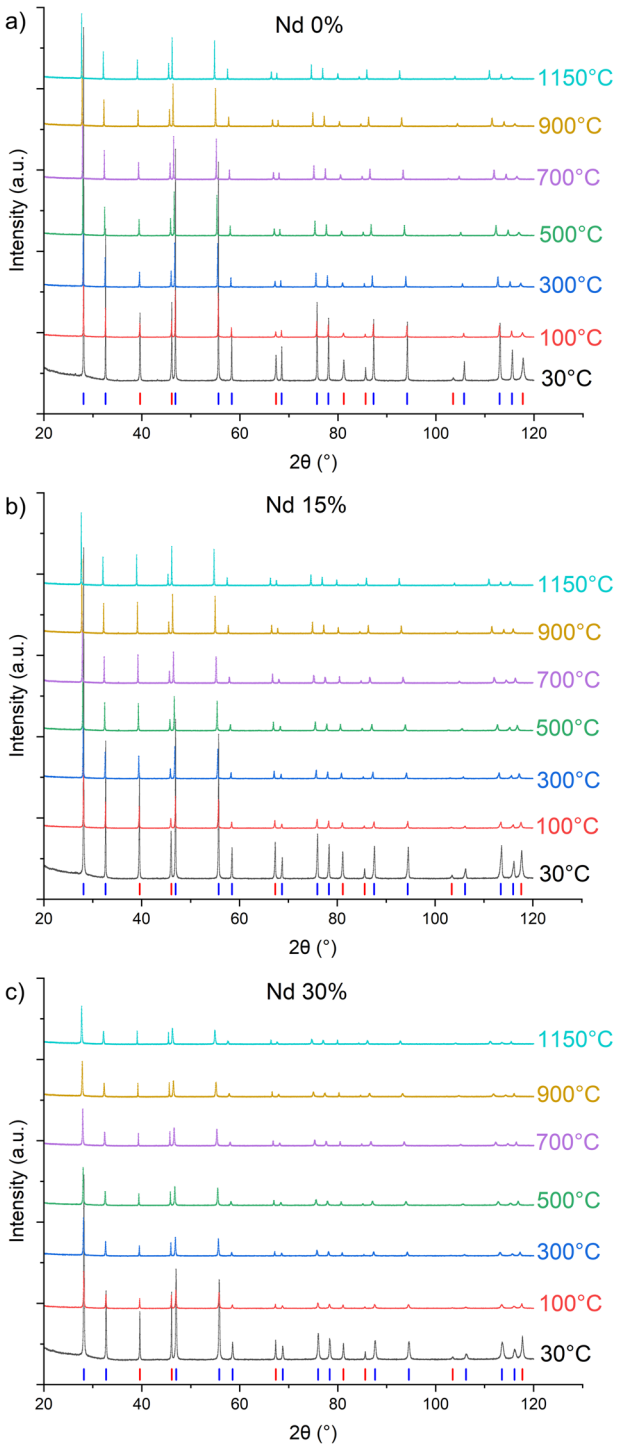


Fig. 3 | VT-XRD results of samples performed under vacuum. VT-XRD diffractograms at different temperatures in vacuum for **a** Nd 0%, **b** Nd 15% and **c** Nd 30%. Allowed reflections of the $Fm\bar{3}m$ space group for fluorite UO_2 and Pt are respectively represented by blue and red markers. With increasing temperature, a shift in the peaks towards lower 2θ values is observed.

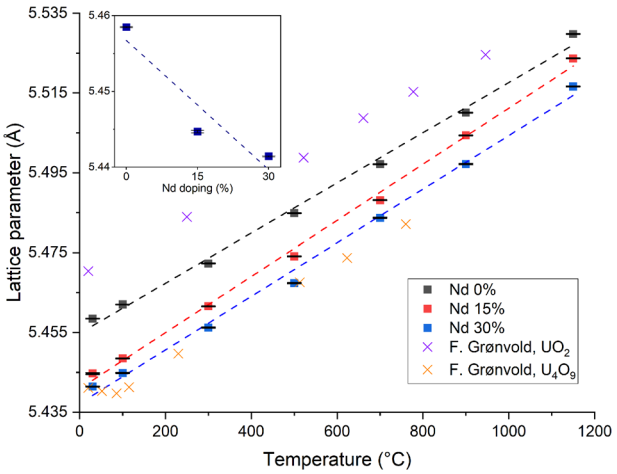


Fig. 4 | Determined lattice parameter values as a function of temperature under vacuum for all samples. Lattice parameter values as a function of temperature in range 30–1150 °C determined by Rietveld analysis for the samples: Nd 0% (black), Nd 15% (red) and Nd 30% (blue), compared to the literature data[77]. The inset in the graph shows the dependence of the lattice parameter on the level of Nd doping in UO_2 at room temperature. Details of the linear fits shown by the dashed lines are provided in Supplementary Information Note 4.

To further probe the suspected speciation of CsI occurring with Nd doping of the investigated materials, XANES measurements were performed on the Cs and I K-edges. Using the K-edge for XANES analysis requires relatively higher X-ray energies (35.9846 keV and 33.1694 keV, respectively) as opposed to other edges. XANES measurements enable the bulk of the material to be appropriately probed, ensuring that associated measurement signals do not arise solely from the surface, as with EDX measurements. The Fig. 6 provides the normalised K-edge XANES spectrograms for Cs and I in the Nd 0% and Nd 15% samples, plotted additionally with a CsI standard.

When the K-edge XANES spectra of Cs and I are considered, subtle but significant variability is observed in the white line shape and shift of the Nd 15% sample compared to the undoped UO_2 sample and also the CsI standard. These results clearly indicate that, firstly, the added CsI has readily dissociated from its original chemical compound state, and secondly, the chemistry of Cs and I differs between the Nd-doped and Nd-free samples, consistent with the SEM-EDX analysis. When the spectra of the two investigated samples are compared, it can be seen that the Nd-bearing sample shows a subtle shift of the white line towards higher energy at both the Cs and I K-edges. If the SEM-EDX measurements are followed, this indicates that partial oxidation of Cs and I is occurring in addition to their speciation. For instance, this could be explained by the presence of Cs-oxide or iodate (IO_3^-) phases, bearing in mind the more ionic nature of CsI. The presence of partially oxidised Cs could be detected in case of the Cs-uranyl compounds formation[59,60], while the partial occurrence of iodate species could potentially be stabilised by uranyl and/or Nd species forming respectively uranyl and Nd-iodates, or by a combination of both[61,62]. In the case of the Nd-free Nd 0% sample, the white line on both the Cs and I K-edges more closely matches the CsI standard, consistent with the SEM-EDX analysis, indicating that speciation has not occurred. Given the low sensitivity at the K-edge, this difference is not considered to be affecting the XANES results. Table 3 shows the positions of the white lines in the Cs and I K-edge XANES spectra. The observed shifts (up to ~0.9 eV at the Cs K-edge and ~1.2 eV at the I K-edge) are larger than the reported experimental resolution or uncertainty (±0.5 eV). These shifts are therefore significant and consistent with a change in the oxidation state of Cs and I in the presence of Nd in the sample, although a contribution from changes in the local coordination/bonding environment cannot be totally discounted. Moreover, these measurements strongly support the SEM-EDX analysis indicating that Nd in the UO_2 structure contributes to the variable speciation of Cs and I.

Cs, I and CsI release studies

In considering the combined SEM-EDX surface analysis with the Cs and I K-edge XANES bulk measurements, the results of the investigation thus far show the addition of Nd into the UO_2 structure directly impacts the speciation of Cs and I. The observation that they exist in different chemical

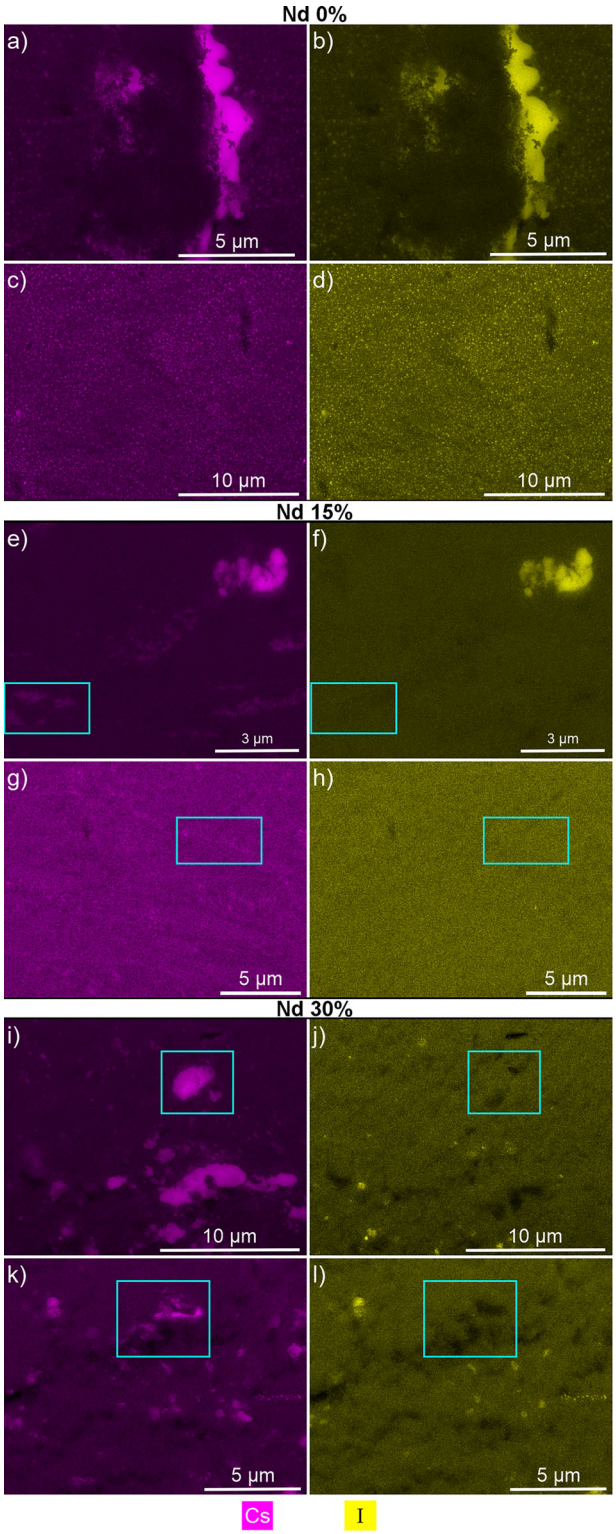


Fig. 5 | I and Cs EDX mapping results for all samples. EDX maps of I and Cs in two distinct locations for the **a**–**d** Nd 0%, **e**–**h** Nd 15% and **i**–**l** Nd 30% samples. The maps show the EDX signal intensity of Cs (purple) and I (yellow) at two different locations on the surface of the pellets' cross section: **a**, **b** (for the Nd 0% sample), **e**, **f** (for the Nd 15% sample) and **i**, **j** (for the Nd 30% sample), where a relatively large particles of CsI were found, and **c**, **d** (for the Nd 0% sample), **g**, **h** (for the Nd 15% sample) and **k**, **l** (for the Nd 30% sample), where CsI is more homogeneously distributed, respectively. While the distribution of Cs and I appears identical in the Nd 0% sample (**a**–**d**), heterogeneities become apparent in the Nd 15% (**e**–**h**) and Nd 30% (**i**–**l**) samples. For reference, teal rectangles highlight some of the mapping regions where the distribution of Cs and I differs.

environments in the different Nd-doped samples suggests that their temperature-induced release should vary accordingly. Consequently, to investigate this hypothesis KEMS measurements were performed under the temperature range of 500–2130 °C. Spectrograms of numerous gaseous species were obtained by vaporising samples in a Knudsen cell with using a mass spectrometer to measure the vapour signal. These species were selected for measurement in advance and included I^+, Cs^+ and CsI^+, among others, which enabled determination of their behaviour during evaporation. Figure 7 shows the raw data on KEMS measured mass spectrometry signal as a function of temperature.

Based on the data in Fig. 7, it is possible to assess qualitative characteristics of the Cs and I release. Three regions stand out from the main observations of the I^+, Cs^+ and CsI^+ curves and from checking the CsI^+/I^+ and CsI^+/Cs^+ ratios (see Supplementary Information Note 7). The first region is up to 1200 °C, where CsI melting occurs (632 °C) and the evaporation of I^+, Cs^+ and CsI^+ gaseous species occurs mainly from the sample surface. The second region is the intermediate range between 1200 °C and 1500 °C, where CsI boiling occurs (1280 °C) and evaporation mainly occurs due to cracking of the sample. The third region is the final release region from 1500 °C, when the sample matrix itself starts to evaporate. The high release in the latter region is explained by the high density of the sintered samples, which hinders gas diffusion at lower temperatures. Consequently, reaching evaporation of the UO_2 matrix exposes the intergranular CsI inclusions, initiating their release.

An important observation here is the difference in the onset temperatures of this final release. The differences between samples Nd 0% and Nd 15% could be explained by different oxygen hyperstoichiometry (see section "Material characterisation. X-ray diffraction"), which is known to promote an earlier release[63]. However, the differences between samples Nd 0% and Nd 30%, the latter of which has lower oxygen hyperstoichiometry, can be explained by the presence and quantity of Nd. Therefore, in addition to its previously described influence on CsI speciation and microstructure, Nd evidently favours a shift in release towards lower temperatures.

The effect of Nd can also be seen in the patterns observed during the final release, including both Cs^+, I^+ and the signals related to the UO_2 matrix. In Nd-free Nd 0% sample in particular, the signals continue to rise sharply even when the maximum measured temperature is reached. However, in the case of the Nd-doped samples, saturation is already observed in Nd 15% sample at this temperature, while in Nd 30% sample the signals reach a plateau. Although not all UO_2-related cation signals were collected for some samples, those that were measured are sufficient to identify differences in final release. The next important observation relates to the CsI^+/I^+ and CsI^+/Cs^+ ratios (see Supplementary Information Note 7). By the time of the final release, the I^+ and Cs^+ converge. However, it was also observed that during final release the CsI^+/I^+ and CsI^+/Cs^+ signal ratios decreased with increasing Nd content. Furthermore, in Nd 30% sample, the I^+ signal becomes higher than the Cs^+ signal. This behaviour suggests that chemical changes occur in the presence of Nd at high temperatures that affect the release of Cs and I. Moreover, although CsI is still present in the samples, the CsI^+/I^+ and CsI^+/Cs^+ signal ratios indicate that in the samples containing Nd, the release of Cs and I does not originate solely from CsI.

Based on the obtained spectrograms, Normalised Instantaneous Release (NIR) and Normalised Fractional Release (NFR) were also calculated in accordance with Eqs. (2) and (3) respectively[34], which should be noted as being simplified for relative qualitative comparison.

$$NIR(t_i) = \frac{I\sqrt{T}}{\max(I\sqrt{T}\forall T)} \tag{2}$$

$$NFR(t_i) = \frac{\int_0^{t_i} I\sqrt{T}dt}{\int_0^{t_{end}} I\sqrt{T}dt} \tag{3}$$

with I – measured mass spectrometry signal, T – temperature, and t_i – time of the recording.

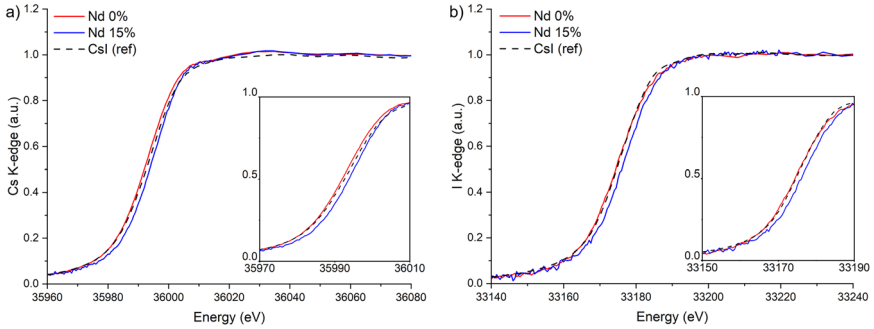


Fig. 6 | Normalised Cs and I K-edge XANES spectra for Nd 0% and Nd 15%. Normalised XANES the K-edge spectra of **a** Cs and **b** I for the Nd 0% (red) and Nd 15% (blue) samples against the CsI (black dashed) standard. The slight shifts in the Nd-doped samples white line occurring for both Cs and I indicate a relatively different chemical environment for these elements compared to the CsI standard and between each sample.

Table 3 | White line positions in the XANES spectra at the Cs and I K-edges

Sample	White line position at Cs K, eV	White line position at I K, eV
Ref CsI	35994.1(5)	33176.2(5)
Nd 0%	35993.2(5)	33176.0(5)
Nd 15%	35994.9(5)	33177.4(5)

The NIR is defined as the differential effusion flow, measured in terms of the amount of vapour species present per unit time at a given temperature, and is subsequently normalised to the highest peak of the given release. The NFR is defined as the integral of the instantaneous release, at a given temperature, which is normalised to the value at the end of the release.

NIR and NFR calculations enable the transition from raw KEMS data to quantitative evaluations of gaseous fraction release from the sample. Figure 8 provides the results of the KEMS data analysis with calculated NIR and NFR of I^+, Cs^+ and CsI^+ gaseous species for all three samples.

The NIR data confirm the previously observed behaviour of I^+, Cs^+ and CsI^+ at UO_2 matrix evaporation temperatures, where the temperatures at which the final evaporation of these gaseous species begins are lower, the more Nd is present. Here, it is also pertinent to consider the spikes in the NIR curves at lower temperatures in Fig. 8. As described in the previous section, the peaks observed below the final release temperature of 1500 °C are attributed to the presence of pure CsI (or other Cs-, I-based compounds) at the surface of the sample as well as to the propagation of cracks in the heated sample, accompanied by a sharp release of exposed material, which can be also seen from the total amount of material in the NFR graph. The significant differences in patterns and quantitative values between the samples further confirm the influence of Nd on the behaviour of Cs and I during release. Furthermore, the similar patterns of I^+, Cs^+, and CsI^+ in the Nd-free sample suggest that these gas fractions mostly originate from CsI particles. Conversely, in the Nd-doped Nd 15% and Nd 30% samples, the normalised release curves of I^+, Cs^+, and CsI^+ differ significantly, especially in the high-temperature region. Such behaviour in Nd-doped samples may indicate the formation of secondary phases caused by reactivity between Cs/I and U/Nd. However, the upper measurement limit of the instrument is 512 amu which limits the ability to measure potential gaseous species such as dicaesium uranate ($Cs_2UO_4^+$, 576 amu) or Nd-iodide (NdI_3^+, 523–527 amu, depending on the Nd isotope), while no other compounds with molecular weights <512 amu were detected. Nevertheless, the results of the KEMS data analysis generally support the observations made by SEM and XANES analysis: the presence of Nd in UO_2 influences the chemistry of Cs and I and further appears to have an impact their thermal release during evaporation depending on the Nd content.

Discussion

This investigation has demonstrated that the incorporation of CsI into $(U_{1-y}Nd_y)O_2$–(CsI) for y = 0, 15 and 30% nanoceramics, synthesised via hydrothermal decomposition and subsequent SPS treatment, is a chemically variant process, whereby increasing amounts of Nd appear to result in increased speciation of CsI. Although the synthesis route and its parameters can influence this effect, optimised control of the SPS process steps and subsequent post-analysis showed that the specimens had comparable characteristics. The observed chemical differences can therefore be attributed primarily to the effect of Nd. Pertinently, via KEMS measurements on these materials it was found that the temperature-induced CsI release correlates with the presence of Nd. Specifically, increasing the Nd concentrations which results in enhanced CsI speciation, translate to a lower temperature at which Cs, I and CsI are released compared to the Nd-free case.

A core component of this investigation has been the synthesis of nanoceramic materials targeted at replicating the structure and chemical properties of the actual HBS occurring in SNF. Accordingly, it is important to contrast and discuss the differences between these systems. Investigating the HBS in SNF is an exceedingly challenging task due to the difficulty of handling irradiated specimens and discerning the complex structural and chemical effects within the HBS against the overall bulk effects of SNF as the HBS is generally observed at the periphery of fuel in post examination studies[7]. In considering grain size variations, our investigated materials (133–557 nm) found good consistency with what has been reported for the HBS, where sizes of 100–500 nm have been observed[7,8]. An oxygen excess was further found in the samples studied, which is largely consistent with the HBS, where generally due to the formation of fission and transmutation products, the O/M ratio shifts towards oxygen hyperstoichiometry[64].

A pertinent difference between the actual HBS and the synthesised materials of this study is their specific ceramic properties: In particular, the formation of the HBS involves rearrangement of the grain structure via fission gas extrusion, leading to the formation of non-connected pores, these effectively reduce the local density of the structure relative to the fresh fuel. However, these pores also act as traps for fission gases, hindering their release[9,11,16,17]. Additionally, radiation damage processes and interstitial lattice defects in the UO_2 HBS matrix lead to significant point defects and dislocation loops that effectively transport newly formed fission gases into the pores of the HBS, resulting in their low concentration in the matrix[65]. In comparison, our investigated synthesised materials show high relative densities which is associated with using SPS to generate the nanostructured ceramic materials without a forming mold[55] and have comparatively a low amount of lattice defects. This heightened density can hinder temperature-induced release of Cs and I, but can also explain the difference in release profiles between the synthesised samples and actual HBS observed in the KEMS analysis[34]. Furthermore, the amount of CsI used in the present study is also considered relatively consistent with that of the HBS. Although sub-molar amounts of Cs and I are reported in bulk SNF, when taken to high burn-up[51–53], the localised increased burn-up within the HBS can lead to values that are commensurate with the present investigation.

An additional key difference between SNF and the material examined in this study is the presence of other fission and transmutation products other than just Nd, Cs, and I. Nd^{3+} is often used as a favourable minor actinide surrogate, particularly for Am^{3+}, where they have similar ionic

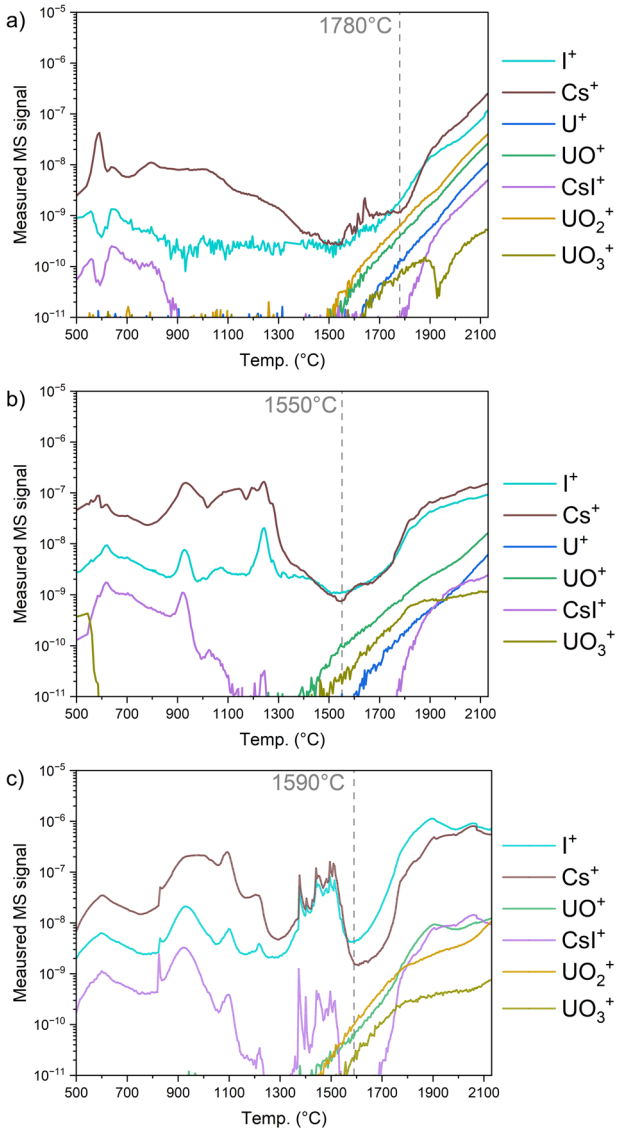


Fig. 7 | Measured KEMS signals obtained for all samples. Measured KEMS signal of various gaseous species as a function of temperature for **a** Nd 0%, **b** Nd 15% and **c** Nd 30%. The grey vertical line indicates the approximate start of the final release of I^+ and Cs^+ caused by evaporation of the UO_2 matrix itself.

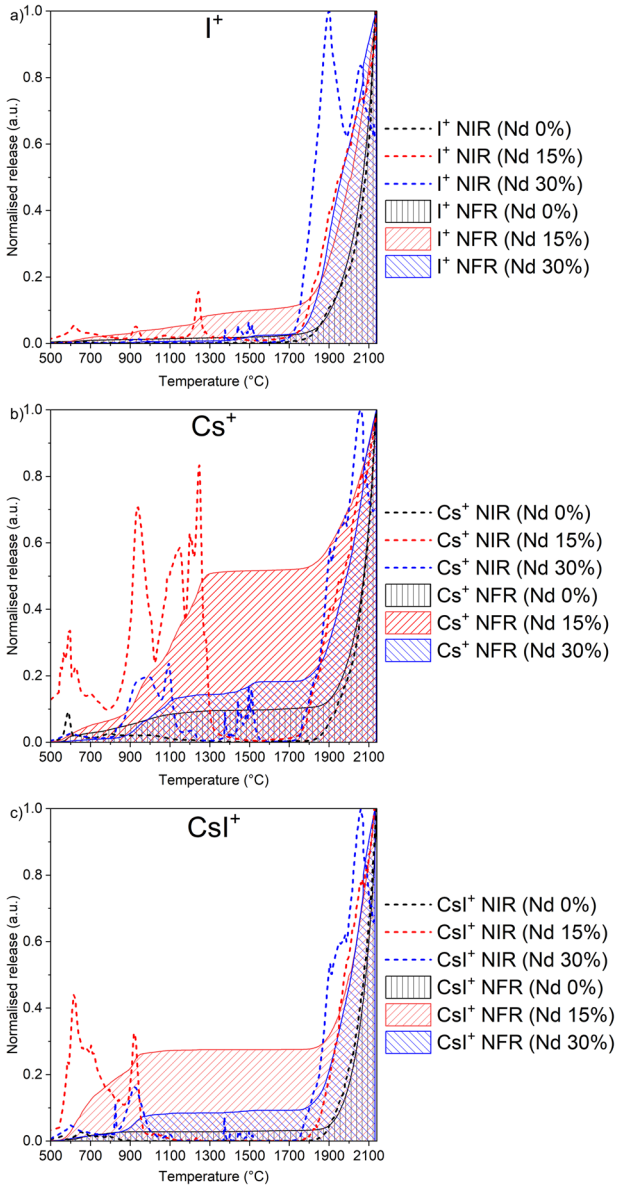


Fig. 8 | NIR and NFR of all samples determined from KEMS measurements. NIR and NFR of **a** I^+, **b** Cs^+ and **c** CsI^+ gaseous species for Nd 0%, Nd 15% and Nd 30% illustrated in black, red and blue respectively.

radii[49], and chemical studies have shown good congruence[42]. Equally, the chemical properties of Nd^{3+} can be readily extended to other *Ln*'s that occur as FPs due to their similar chemistries. These, and the minor actinides, when trivalent, are expected to enter solid solution with UO_2. Differences are naturally found when the actinide case is more specifically considered regarding redox, for instance Am can occur as Am^{4+} in fuel and react with the Zircaloy cladding material[42]. Nevertheless, the materials synthesised in the investigation do provide a good model to examine the structural and chemical effects of the HBS, particularly in the core focus of CsI speciation and temperature-induced release.

This investigation highlights the key role of Nd doping, and of the associated chemical and microstructural changes in the synthesised nano-ceramics, in CsI speciation and temperature-induced release. It is therefore important to consider the potential chemical origins of how this solid solution behaviour affects release. For higher Nd doping, the speciation observed for CsI indicates that it can form chemically distinct phases whereby the potential formation of secondary phases containing Cs and I may arise due to their reactivity with elements of the UO_2 matrix (Nd and U) and subsequent precipitation. The incorporation of Cs and I within the UO_2 matrix is largely ruled out as a leading effect, due to their known low solubilities. Some studies have proposed the possible reactivity of Cs with U forming Cs_2UO_x phases from thermodynamic calculations and experimental observations[59,60,66]. The free I produced via this pathway could either evaporate as $I_2 \uparrow$, react with Nd to form intermetallic NdI_3, or other mixed U/Nd-based intermetallic or oxide compounds. Subsequently, chemical reactivity with Nd can also be expected particularly since, despite the formation of a solid solution between Nd and UO_2, a recent pre-print[67] at the time of writing has shown that Nd tends to migrate towards grain boundaries, where it may react with Cs/I. Crucially, nano-sized grains, as found in HBS, amplify this effect by reducing the migration distance to the boundary. Thus, enhancing surface reactivity between Nd and Cs/I. Furthermore, the presence of a trivalent *Ln's* in UO_2 is known to result in a general increase of the oxygen potential in the context of fuel[68]. With regard to general model materials, during long in-furnace sintering, the oxygen potential of the sample and the sintering atmosphere tend to equilibrate[69]; however, in the case of relatively rapid SPS, such equilibrium might not be reached and the oxygen potential of the samples is dictated by the chemistry of the dopant

rather than the sintering atmosphere, concordant to the behaviour in fuel. Consequently, as the Nd-doping level increased, the oxygen potential of the samples is raised. This may consequently be an indirect contributing factor of the Nd occurrence leading to the oxidation-based CsI speciation with the further potential reactivity between U/Nd and Cs/I[66]. In addition to the potential formation of phases via such reactivity, there is also the possibility of Nd influencing CsI through van der Waals forces. These effects arise because Cs and I are both heavy, highly polarisable ions[70] and van der Waals dispersion between such species is non-negligible compared to the total cohesive energy in soft ionic lattices and related materials. Critically these forces directly impact detachment and release at specific temperatures. Changes to the chemical structure of the UO_2 lattice, such as via the aliovalent substitution of U^{4+} for Nd^{3+} generating U^{5+} can readily result in a change to the van der Waals interactions, and this effect is also amplified by the migration of Nd to the boundaries of the nanograins. It is conceivable that such concentrations of Nd along the surface of the UO_2 nanograins which contact CsI can impact the van der Waals interactions leading to modulation of the CsI bonding and subsequent speciation. Particularly, Nd^{3+} would be expected to lower the local charge density when found more concentrated on the surface of the nanograins than U^{4+}, leading to reduced interactions and retention with I^-.

It is noteworthy that the amount of Nd directly influences the microstructure, particularly grain size of the precursor powder material prior to SPS (see Supplementary Information Note 3). Specifically, as the content of Nd increases, there is a reduction in grain size of the examined materials, this can in turn affect the oxygen uptake and stoichiometry of materials. However, oxygen stoichiometry calculations showed similar values, with relatively marginal discrepancy, and consistent VT-XRD behaviour. Nevertheless, the use of high doping amounts of Nd is a more prominent and considered major variable between the examined samples. Accordingly, the speciation of CsI can result from of a variety of factors, critically however, these are driven by the chemistry and inclusion of Nd in the materials.

Previous studies that have used KEMS measurements to investigate the temperature-induced release of CsI from UO_2 model materials sintered using SPS showed a single early release of Cs and I (in the range of 530 to 1130 °C)[28,35]. However, these studies did not focus on nanoceramics, where the average grain sizes were an order of magnitude larger than that of the materials investigated here[45]. Smaller grain sizes should result in faster CsI release due to a much higher grain boundary density. Additionally, these studies did not examine effects associated with Nd or related UO_2 lattice matrix-soluble elements via model materials. In those investigations, lower-temperature release of the matrix was generally observed for the SPS-synthesised UO_2 materials compared to the present study. Notably, this appears to be the first study to have examined the effect of UO_2 nanoceramics on CsI, in addition to Nd incorporated as a solid solution. Compared to the aforementioned model system studies, final CsI release occurs at comparatively higher temperatures (without considering Nd). This could be attributed to the effect of nanograins, but is likely more related to more compacted material, which retains CsI within the structure slowing its release up to high temperatures. When considering the effect of Nd in the present investigation and taking into account that the synthesised compounds have similar densities, differences are observed between when Nd is present or absent. Particularly, the samples Nd 15% and Nd 30% possess obviously non-coincident I^+, Cs^+, and CsI^+ release behaviour that is not found in the release spectrum of the Nd-free Nd 0% sample. This could indicate the release occurring from Cs- and I-based compounds formed as a result of the reactivity between these elements with Nd or U. Another important observation is that the final release of all the gaseous species measured shifts towards lower temperatures as the Nd content increases. Studies on the vaporisation of irradiated nuclear fuel with high burn-up (55–67 GWd/tHM) show that the release profiles of I and Cs exhibit greater release at higher temperatures (>1230 °C)[28], which is pertinently closer to the Nd-doped compositions of the present investigation. Previous work on very high burn-up SNF (240 GWd/tHM) demonstrated that the release patterns of Cs and I measured by KEMS exhibited a more similar behaviour and two peaks: in the region of ~730 °C and of ~1230 °C, similar to the findings in the present study[38]. However, the temperature-induced release of IRF-related elements is influenced by a multitude of factors inherent in the complexity of SNF, for instance, arising from the fuel's irradiation history, as well as its chemical, microstructural, thermal, and physical characteristics. Decoupling these effects and cross-comparing SNF specimens towards determining underlying chemical-physical mechanisms is extremely difficult from a direct investigative perspective. Nevertheless, the current investigation builds upon previous studies of CsI-included UO_2 model material works by doping with Nd as a proxy for examining the behaviour of matrix-soluble minor actinides and FPs, and simultaneously incorporating the microstructural effects of a nanomaterials, like that found in the actual HBS. Consequently, the results show more agreement with that of higher burn-up irradiated fuel studies. Although γ-radiation is expected to drive CsI speciation[28,29], this study has demonstrated that it is not the only source. Chemical processes within irradiated fuel, particularly in HBS regions also impact the chemistry and subsequent release of Cs, I, and potentially other IRF-related elements. This naturally has pertinent implications for the use and storage of nuclear fuel, particularly of which are intended for high burn-up cycles, that is currently being pursued by many nations.

Conclusions

This investigation has examined the chemistry of CsI within SPS-synthesised CsI-bearing UO_2 nanoceramics through Nd doping variation towards replicating the conditions of the HBS in irradiated nuclear fuel with high burn-up. The results demonstrated the gradual and continual speciation of CsI as a result of Nd incorporation within the bulk material which subsequently affects the temperature-induced release of I^+, Cs^+ and CsI^+. As shown by a combination of Cs and I K-edge XANES spectroscopy and SEM-EDX analysis, CsI in presence of Nd is found to speciate into individual phases. Considering the chemistry of the materials it is suspected Cs and I adopt phases that are either separate, oxidised or involve the reactivity with the Nd-doped UO_2 lattice matrix. KEMS measurements and analysis provided release spectrums from examined compositions, where the temperature of final release of I^+, Cs^+, and CsI^+ gaseous species is shifted towards lower temperatures with increasing Nd content. Additionally, the release profiles indicate they possess features which are consistent with non-CsI species, such as secondary phases arising from initial speciation and reactivity. When the results are compared with previous CsI release studies in model materials[28,35] and irradiated fuel[28,38], more agreement is found with the latter. It has been previously established that γ-radiation induces speciation of CsI within SNF which subsequently affects its release[28]. The present study has demonstrated that CsI stability and speciation are not only radiologically, but also chemically affected, within the UO_2 matrix resembling that of the HBS. This work provides critical fundamental understanding into the behaviour of CsI within high burn-up irradiated fuel and how changes to the local chemistry and microstructure of the fuel, via the formation of the HBS and subsequent enhanced FPs inventory, can affect the release mechanisms of IRF-related elements including Cs and I, which constitutes a crucial aspect of SNF management safety.

Methods

Materials and synthesis

A hydrothermal decomposition method, derived from a previously reported one[71], was used for the synthesis of UO_2 and Nd-doped UO_2 nanopowder precursor material. A $Nd(NO_3)_3{\cdot}6H_2O$ solution, produced by dissolving Nd_2O_3 (Alfa Aesar, 99.9%) in nitric acid, was mixed with a $UO_2(NO_3)_2{\cdot}6H_2O$ solution stoichiometrically for targeted final $(U_{1-y}Nd_y)O_2$ compositions of y = 0, 15 and 30 mol%. To these solutions, hydrazinium hydroxide N_2H_5OH (Sigma-Aldrich, about 100%) was added triggering a rapid precipitation consistent with literature[71]. The mixtures were placed in a 100 ml autoclave (model 4793, *p-T* controlled, Parr Instruments Company, USA) with a Teflon inset, where deionised water was added so that the remaining free volume was 35 ml and the pH of the

final mixtures was found to be ~9.5 in all samples. The hermetically sealed mixtures were then heated to 180 °C and held at this constant temperature for five hours, after which the mixture was cooled to room temperature at a rate of ~2.5 °C/min. The peak excess pressure was in range of 20–30 bar. The resulting suspension was dried at room temperature in argon until the liquid had completely evaporated, after which all samples were reduced in an atmosphere of Ar/6.5% H_2 ~ 1 l/min in a furnace, that was heated to a temperature of 500 °C at a rate of 100 °C/h, held for 4 h, and then cooled to room temperature at a rate of 200 °C/h. The samples were then manually mixed with CsI powder (Suprapure®, Merck) in a mortar in a glove box. Taking into account that some of the CsI would evaporate during SPS[45], initially 3 mol % of CsI was mixed into the UO_2.

Spark plasma sintering

$(U_{1-y}Nd_y)O_2$–(CsI) powder mixtures were placed in portions of ~300 mg in a graphite die, pre-pressed at 17.7 MPa and loaded into a SPS furnace (FCT Systeme GmbH, Rauenstein, Germany) installed in a glove box[72]. As the final microstructure of the samples, as well as CsI evaporation, are affected by the SPS sintering temperature and dwell time, several optimisation runs were performed to select suitable SPS parameters in order to ensure comparability between examined samples. These are discussed in the results section. The sintered test samples were examined using scanning electron microscopy (SEM, details in the respective section) to verify the grain size and the homogeneity of the CsI particles distribution. The following optimised SPS parameters were selected for the synthesis of subsequently investigated materials: heating in an argon atmosphere at a rate of 100 °C/min to 950 °C under a uniaxial pressure of 70.7 MPa, a dwell time of 5 s, cooling to 400 °C at a rate of 200 °C/min and, after reducing the pressure to 17.7 MPa, followed by cooling down to room temperature without any controlled cooling. Sintered ceramic specimens were recovered for subsequent analysis. The densities of the samples were measured using Archimedes' principle involving immersing the samples in water. The grain sizes of around one hundred individual grains were measured using images obtained by SEM analysis. Their sizes were estimated with an average value determined and an uncertainty provided based on a ½ standard deviation made across the range of data collected. The molar concentration of elements in the sintered samples was determined and verified using inductively coupled plasma mass spectrometry, ICP-MS (Thermo Element2, Thermo Electron Corporation, Germany), with a developed methodology[73].

Variable temperature X-ray powder diffraction

To confirm the phase composition, probe for chemical decomposition and structural changes at elevated temperatures, variable temperature X-ray powder diffraction (VT-XRD) was performed using a Bruker D8 Advance diffractometer with Bragg–Brentano (θ/2θ) geometry, equipped with a Kα1 monochromator and a Lynxeye detector. During the measurements a vacuum atmosphere was used. Diffractograms were collected for each sample that were mounted on platinum (Pt) holders at an ambient temperature of 30 °C, followed by heating at the following temperature steps: 100, 300, 500, 700, 900 and 1150 °C. The data were collected in the 2θ range of 20–120°, and the diffractograms were analysed in the 2θ range of 20–70° using the Rietveld method as implemented in GSAS-II software[74].

Electron microscopy

The microstructure of the samples produced and trialled during the SPS parameter optimisation and initial microstructure examination, as well as the inspection of pre-sintered powders, were performed with SEM using a VEGA electron microscope (Tescan, Czech Republic) equipped with an Everhart-Thornley Detector (ETD) at 30 kV. The morphology of the sintered pellets was examined using an Apreo 2 C LoVac electron microscope (ThermoFisher Scientific, Netherlands), which was also used for EDX mapping (Octane elect PLUS Silicon Drift Detector, EDAX, Weiterstadt, Germany) at 20 kV. For this purpose, pellet fragments with relatively flat pellet cross-section surfaces were selected. EDX maps were collected with an accelerating voltage of 20 kV, which focused on the edges: I L-edge, Cs L-edge, Nd L-edge, O K-edge, C K-edge and U M-edge. Additionally, spot EDX measurements were performed to analyse various microparticles and impurities found on the unpolished cross-sectional surface. Supplementary Information Table S1 in Note 1 provides specific spot measurement results for determining Cs/I ratios in each sample.

X-ray absorption spectroscopy near edge structure

XANES measurements on the Cs and I K-edges were performed at the ROBL[75] beamline at the ESRF in Grenoble, France. The incident energy was scanned using a water-cooled Si(111) double monochromator around the corresponding edge. Two Pt mirrors, positioned before and after the monochromator, were used to collimate the beam, reject higher harmonics, and focus it on the sample. Prior to measurement, the samples were ground into a powder, mixed with boron nitride at a weight ratio of 1:10, and then pressed into pellets. The spectra were collected at ambient temperature using an 18-element solid-state germanium detector (Ultra-LEGe, GUL0055, Mirion Technologies). The detector was tuned to the maximum intensity of the emission line of the corresponding in non-resonant mode (incident energy above the corresponding edge). All measurements were performed at 25 °C. For the spectroscopy, the UO_2–(CsI) and $(U_{0.85}Nd_{0.15})O_2$–(CsI) samples were chosen. Due to sample restrictions relating to the radioactive nature of the samples, the $(U_{0.7}Nd_{0.3})O_2$–(CsI) sample could not be transported and measured.

Knudsen effusion mass spectrometry

The behaviour of Cs and I during evaporation was analysed using a Knudsen effusion mass spectrometer, which was placed in an α-tight and lead-shielded glove box. The Knudsen cell consisted of a small tungsten crucible, positioned inside a high-temperature furnace and coupled to a QMG422 quadrupole mass spectrometer (Pfeiffer Vacuum GmbH, Germany)[76], which was equipped with a cross beam electron bombardment ion source. An electron energy of around 32 eV was selected for ionisation, striking a balance between avoiding excessive dissociation and achieving sufficient ionisation efficiency. The spectra were recorded in a temperature range from 500 to 2130 °C, with a constant linear heating rate of approximately 7 °C/min with a recording speed of 1 s/mass. Although the device can measure species up to 512 amu, this study focused primarily on $^{127}I^+$, $^{133}Cs^+$, $^{133}Cs^{127}I^+$, $^{238}U^+$, $^{238}U^{16}O^+$, $^{238}U^{16}O_2^+$ and $^{238}U^{16}O_3^+$ ionic species with additional recorded masses that are available in Supplementary Information Note 2. Silver (Ag) was used as the reference material because its gaseous species are inert towards the analysed gas fractions. Due to instrument access issues not all U-based species for the samples could be appropriately measured.

Data availability

The authors declare that all data supporting the findings of this study are available within the manuscript and the Supplementary Information file. The corresponding authors are available to provide all data upon reasonable request.

Received: 7 July 2026; Accepted: 6 October 2026;
Published online: 30 October 2026

References

1. Karoutas, Z. et al. The maturing of nuclear fuel: Past to Accident Tolerant Fuel. *Prog. Nucl. Energ.* **102**, 68–78 https://doi.org/10.1016/j.pnucene.2017.07.016 (2018).
2. Kashibe, S. & Une, K. Effect of additives (Cr_2O_3, Al_2O_3, SiO_2, MgO) on diffusional release of ^{133}Xe from UO_2 fuels. *J. Nucl. Mater.* **254**, 234–242 https://doi.org/10.1016/S0022-3115(97)00356-5 (1998).
3. Arborelius, J. et al. Advanced doped UO_2 pellets in LWR applications. *J Nucl Sci Technol* **43**, 967–976 https://doi.org/10.3327/jnst.43.967 (2006).

4. Cole, S. E., Delafoy, C., Graebert, R., Louf, P. H. & Teboul, N. AREVA optimized fuel rods for LWRs. *TopFuel*, *Manchester, UK*, 520–529 (2012).
5. Lassmann, K., Walker, C. T., Vandelaar, J. & Lindstrom, F. Modeling the high burnup UO_2 structure in LWR fuel. *J. Nucl. Mater.* **226**, 1–8 https://doi.org/10.1016/0022-3115(95)00116-6 (1995).
6. Sonoda, T. et al. Transmission electron microscopy observation on irradiation-induced microstructural evolution in high burn-up UO_2 disk fuel. *Nucl. Instrum. Methods Phys. Res. B: Beam Interact. Mater. At.* **191**, 622–628 https://doi.org/10.1016/S0168-583x(02)00622-5 (2002).
7. Rondinella, V. V. & Wiss, T. The high burn-up structure in nuclear fuel. *Mater. Today* **13**, 24–32 https://doi.org/10.1016/S1369-7021(10)70221-2 (2010).
8. Johnson, L., Ferry, C., Poinssot, C. & Lovera, P. Spent fuel radionuclide source-term model for assessing spent fuel performance in geological disposal. Part I: assessment of the instant release fraction. *J. Nucl. Mater.* **346**, 56–65 https://doi.org/10.1016/j.jnucmat.2005.04.071 (2005).
9. Mogensen, M., Pearce, J. H. & Walker, C. T. Behaviour of fission gas in the rim region of high burn-up UO_2 fuel pellets with particular reference to results from an XRF investigation. *J. Nucl. Mater.* **264**, 99–112 https://doi.org/10.1016/S0022-3115(98)00474-7 (1999).
10. Barner, J. O., Cunningham, M. E., Freshley, M. D. & Lanning, D. D. High Burnup Effects Program – Final Report [HBEP-61(3P27)]. Report No. DOE/NE/34046-1, (Battelle, Pacific Northwest Laboratories, Pacific Northwest National Laboratory (PNNL), Richland, WA, United States, 1990).
11. Rest, J. et al. Fission gas release from UO_2 nuclear fuel: a review. *J. Nucl. Mater.* **513**, 310–345 https://doi.org/10.1016/j.jnucmat.2018.08.019 (2019).
12. Noirot, J. et al. High burnup changes in UO_2 fuels irradiated up to 83 GWd/t in M5® claddings. *Nucl. Eng. Technol.* **41**. https://doi.org/10.5516/NET.2009.41.2.155 (2009).
13. Nogita, K. & Une, K. Radiation-induced microstructural change in high burnup UO_2 fuel pellets. *Nucl. Instrum. Methods Phys. Res. Sect. B: Beam Interact. Mater. At.* **91**, 301–306 https://doi.org/10.1016/0168-583x(94)96235-9 (1994).
14. Nogita, K. & Une, K. Irradiation-induced recrystallization in high burnup UO_2 fuel. *J. Nucl. Mater.* **226**, 302–310 https://doi.org/10.1016/0022-3115(95)00123-9 (1995).
15. Gerczak, T. J., Parish, C. M., Edmondson, P. D., Baldwin, C. A. & Terrani, K. A. Restructuring in high burnup UO_2 studied using modern electron microscopy. *J. Nucl. Mater.* **509**, 245–259 https://doi.org/10.1016/j.jnucmat.2018.05.077 (2018).
16. Fast/Instant Release of Safety Relevant Radionuclides from Spent Nuclear Fuel FIRST-Nuclides. Final scientific report. Report No. 5.13, (Collarborative project, Karlsruhe, Germany, 2014).
17. Park, G. I. et al. Cesium release behavior during the themal treatment of high burn-up spent PWR Fuel. *J. Korean Radioact. Waste Soc.* **5**, 53–64 (2007).
18. Konings, R. J. M., Wiss, T. & Beneš, O. Predicting material release during a nuclear reactor accident. *Nat. Mater.* **14**, 247–252 https://doi.org/10.1038/nmat4224 (2015).
19. Johnson, L. H. et al. Spent Fuel Evolution under Disposal Conditions: Synthesis of Results from the EU Spent Fuel Stability (SFS) Project. Report No. NTB 04-09, (National Cooperative for the Disposal of Radioactive Waste (NAGRA), Wettingen, Switzerland, 2005).
20. Nordström, E. Fission gas release data for Ringhals PWRs. Report No. TR-09-26, (Swedish Nuclear Fuel and Waste Management Co (SKB), Stockholm, Sweden, 2009).
21. Tonks, M. et al. Unit mechanisms of fission gas release: current understanding and future needs. *J. Nucl. Mater.* **504**, 300–317 https://doi.org/10.1016/j.jnucmat.2018.03.016 (2018).
22. Johnson, L., Garisto, N. & Stroes-Gascoyne, S. Used fuel dissolution studies in Canada. *Waste Manag.* **85**, 479–481 (1985).
23. Kleykamp, H. The chemical-state of the fission-products in oxide fuels. *J. Nucl. Mater.* **131**, 221–246 https://doi.org/10.1016/0022-3115(85)90460-X (1985).
24. Ferry, C. et al. Synthesis on the spent fuel long term evolution. Report No. CEA-R-6084, (Commissariat à l'Énergie Atomique, Saclay, France, 2005).
25. Finn, P. A., Hoh, J. C., Wolf, S. F., Slater, S. A. & Bates, J. K. The release of uranium, plutonium, cesium, strontium, technetium and iodine from spent fuel under unsaturated conditions. *Radiochim. Acta* **74**, 65–71 https://doi.org/10.1524/ract.1996.74.special-issue.65 (1996).
26. Besmann, T. M. & Lindemer, T. B. Chemical thermodynamics of the system Cs-U-Zr-H-I-O in the light water reactor fuel-cladding gap. *Nucl. Technol.* **40**, 297–305 https://doi.org/10.13182/NT78-A26727 (1978).
27. Spahiu, K. EURAD. State of the Knowledge (SoK) Report. Spent Nuclear Fuel. Report No. Domain 3.1.1, (Swedish Nuclear Fuel and Waste Management Co (SKB) and Chalmers University of Technology, Gothenburg, Sweden, 2021).
28. Colle, J. Y. et al. Cesium and iodine speciation in irradiated UO_2 fuel. *J. Nucl. Mater.* **608**, 155715 https://doi.org/10.1016/j.jnucmat.2025.155715 (2025).
29. Cubicciotti, D. & Davies, J. H. The release of iodine from iodide salts by gamma radiolysis. *Nucl. Sci. Eng.* **60**, 314–319 https://doi.org/10.13182/NSE76-A26888 (1976).
30. Serrano-Purroy, D. et al. Instant release fraction and matrix release of high burn-up UO_2 spent nuclear fuel: effect of high burn-up structure and leaching solution composition. *J. Nucl. Mater.* **427**, 249–258 https://doi.org/10.1016/j.jnucmat.2012.04.036 (2012).
31. Schreinemachers, C. et al. Caesium and iodine release from spent mixed oxide fuels under repository relevant conditions: Initial leaching results. *MRS Adv.* **7**, 100–104 https://doi.org/10.1557/s43580-022-00220-7 (2022).
32. Johnson, L. et al. Rapid aqueous release of fission products from high burn-up LWR fuel: experimental results and correlations with fission gas release. *J. Nucl. Mater.* **420**, 54–62 https://doi.org/10.1016/j.jnucmat.2011.09.007 (2012).
33. Park, G. I. et al. Hot experiment on fission gas release behavior from voloxidation process using spent fuel. Report No. KAERI/TR-3448/2007, (Korea Atomic Energy Research Institute (KAERI), Daejeon, Republic of Korea, 2007).
34. Colle, J. Y. et al. Comparative study of fission product release of homogeneous and heterogeneous high-burn up MOX fuel by Knudsen Effusion Mass Spectrometry supported by EPMA, SEM/TEM and thermal diffusivity investigations. *J. Nucl. Mater.* **578**, 154340 https://doi.org/10.1016/j.jnucmat.2023.154340 (2023).
35. Di Lemma, F. G., Colle, J. Y., Rasmussen, G. & Konings, R. J. M. Fission product partitioning in aerosol release from simulated spent nuclear fuel. *J. Nucl. Mater.* **465**, 127–134 https://doi.org/10.1016/j.jnucmat.2015.06.002 (2015).
36. Colle, J. Y., Hiernaut, J. P., Papaioannou, D., Ronchi, C. & Sasahara, A. Fission product release in high-burn-up UO_2 oxidized to U_3O_8. *J. Nucl. Mater.* **348**, 229–242 https://doi.org/10.1016/j.jnucmat.2005.09.024 (2006).
37. Hiernaut, J. P., Wiss, T., Papaioannou, D., Konings, R. J. M. & Rondinella, V. V. Volatile fission product behaviour during thermal annealing of irradiated UO_2 fuel oxidised up to U_3O_8. *J. Nucl. Mater.* **372**, 215–225 https://doi.org/10.1016/j.jnucmat.2007.03.174 (2008).
38. Hiernaut, J. P. et al. Fission product release and microstructure changes during laboratory annealing of a very high burn-up fuel specimen. *J. Nucl. Mater.* **377**, 313–324 https://doi.org/10.1016/j.jnucmat.2008.03.006 (2008).
39. Kegler, P. et al. Chromium doped UO_2-based ceramics: synthesis and characterization of model materials for modern nuclear fuels. *Materials* **14**. https://doi.org/10.3390/ma14206160 (2021).

40. Murphy, G. L. et al. Deconvoluting Cr states in Cr-doped UO_2 nuclear fuels via bulk and single crystal spectroscopic studies. *Nat. Commun.* **14**. https://doi.org/10.1038/s41467-023-38109-0 (2023).
41. Murphy, G. L. et al. The role of redox and structure on grain growth in Mn-doped UO_2. *Commun. Mater.* **5**, 274 https://doi.org/10.1038/s43246-024-00714-x (2024).
42. Murphy, G. L. et al. Structural and chemical insights on the incorporation of americium into zircaloy-derived monoclinic zirconia. *Commun. Chem.* **9**, 50 https://doi.org/10.1038/s42004-025-01857-9 (2025).
43. Shirokiy, D. et al. Speciation and radiation stability of Cr and *Ln* "Grey-Phases" within Cr-doped (*Ln*,U)O_2 spent fuel model materials. *Npj Mat. Degrad.* **10**. https://doi.org/10.1038/s41529-026-00752-5 (2026).
44. Ge, L., Subhash, G., Baney, R. H. & Tulenko, J. S. Influence of processing parameters on thermal conductivity of uranium dioxide pellets prepared by spark plasma sintering. *J. Eur. Ceram. Soc.* **34**, 1791–1801 https://doi.org/10.1016/j.jeurceramsoc.2014.01.018 (2014).
45. Wangle, T., Tyrpekl, V., Cologna, M. & Somers, J. Simulated UO_2 fuel containing CsI by spark plasma sintering. *J. Nucl. Mater.* **466**, 150–153 https://doi.org/10.1016/j.jnucmat.2015.07.030 (2015).
46. Zhao, D. et al. Effects of porosity and Cr_2O_3 doping on transient behavior of high-burnup UO_2 under simulated RIA/LOCA. *J. Am. Ceram. Soc.* **108**, e20699 https://doi.org/10.1111/jace.20699 (2025).
47. Vinograd, V. L., Bukaemskiy, A. A., Modolo, G., Deissmann, G. & Bosbach, D. Thermodynamic and structural modelling of non-stoichiometric *Ln*-doped UO_2 solid solutions *Ln* = {La, Pr, Nd, Gd}. *Front. Chem.* **9** https://doi.org/10.3389/fchem.2021.705024 (2021).
48. Shannon, R. D. Revised effective ionic-radii and systematic studies of interatomic distances in halides and chalcogenides. *Acta Crystallogr. A* **32**, 751–767 https://doi.org/10.1107/S0567739476001551 (1976).
49. Williams, H. R. et al. Metal matrix composite fuel for space radioisotope energy sources. *J. Nucl. Mater.* **433**, 116–123 https://doi.org/10.1016/j.jnucmat.2012.09.030 (2013).
50. Raiwa, M., Savina, M. R., Roberts, A. G., Shulaker, D. Z. & Isselhardt, B. H. Actinide elemental ratios of spent nuclear fuel samples by resonance ionization mass spectrometry. *J. Am. Soc. Mass Spectr.* **35**, 3233–3241 https://doi.org/10.1021/jasms.4c00371 (2024).
51. webKORIGEN++: Web-Interface for KORIGEN Calculations. Version: 2026.07.17. Karlsruhe Institute of Technology (KIT), <https://nucleonica.com/Application/webKORIGEN/KorigenPlus.aspx> (Accessed 02 September 2026).
52. Daniels, N., Bukaemskiy, A., Poonoosamy, J., Deissmann, G. & Bosbach, D. Verbundprojekt VESPA II: Verhalten langlebiger Spalt- und Aktivierungsprodukte im Nahfeld von Endlagern unterschiedlicher Wirtsgesteine und Möglichkeiten ihrer Rückhaltung, Teilprojekt D. Report No. 02E11607D, (Forschungszentrum Jülich GmbH, Jülich, Germany, 2022).
53. Momotov, V. N., Erin, E. A., Volkov, A. Y. & Kupriyanov, V. N. Post-radiation radiochemical analysis of spent nuclear fuel from VVER-440 reactor. *Radiochemistry* **63**, 197–208 https://doi.org/10.1134/S1066362221020107 (2021).
54. Herrero, B. et al. Charge compensation mechanisms in Nd-doped UO_2 samples for stoichiometric and hypo-stoichiometric conditions: Lack of miscibility gap. *J. Nucl. Mater.* **539** https://doi.org/10.1016/j.jnucmat.2020.152276 (2020).
55. De Bona, E. et al. Single-step, high pressure, and two-step spark plasma sintering of UO_2 nanopowders. *J. Eur. Ceram. Soc.* **41**, 3655–3663 https://doi.org/10.1016/j.jeurceramsoc.2021.01.020 (2021).
56. Tyrpekl, V. et al. On the role of the electrical field in spark plasma sintering of UO_{2+x}. *Sci. Rep.* **7**, 46625 https://doi.org/10.1038/srep46625 (2017).
57. Lee, S. M., Knight, T. W., Voit, S. L. & Barabash, R. I. Lattice parameter behavior with different Nd and O concentrations in $(U_{1-y}Nd_y)O_{2\pm x}$ solid solution. *Nucl. Technol.* **193**, 287–296 https://doi.org/10.13182/nt14-136 (2016).
58. Ohmichi, T., Fukushima, S., Maeda, A. & Watanabe, H. On the relation between lattice-parameter and O/M ratio for uranium-dioxide trivalent rare-earth-oxide solid-solution. *J. Nucl. Mater.* **102**, 40–46 https://doi.org/10.1016/0022-3115(81)90544-4 (1981).
59. Cordfunke, E. H. P., Vanegmond, A. B. & Vanvoorst, G. Investigations on cesium uranates .1. characterization of phases in Cs-U-O System. *J. Inorg. Nucl. Chem.* **37**, 1433–1436 https://doi.org/10.1016/0022-1902(75)80785-8 (1975).
60. Rochedy, M. et al. Comparative study of the I-UO_2 and Cs-UO_2 systems under conditions representative of irradiated fuel. *J. Nucl. Mater.* **620**, 156348 https://doi.org/10.1016/j.jnucmat.2025.156348 (2025).
61. Chen, X. A., Xue, H. P., Chang, X. N., Zang, H. G. & Xiao, W. Q. Hydrothermal synthesis and crystal structures of $Nd(IO_3)_3$ and $Al(IO_3)_3$. *J. Alloy Compd.* **398**, 173–177 https://doi.org/10.1016/j.jallcom.2005.01.050 (2005).
62. Murphy, G. L. et al. The first actinide polyiodate: a complex multifunctional compound with promising X-ray luminescence properties and proton conductivity. *Chem. Commun.* **57**, 496–499 https://doi.org/10.1039/d0cc06835g (2021).
63. Beneš, O., Konings, R. J. M. & Colle, J. Y. Determination of oxygen stoichiometry of oxide fuel during high temperature vapour pressure measurement. *J. Nucl. Mater.* **462**, 182–190 https://doi.org/10.1016/j.jnucmat.2014.12.040 (2015).
64. Une, K. & Oguma, M. Oxygen potentials of UO_2 fuel simulating high burnup. *J. Nucl. Sci. Technol.* **20**, 844–851 https://doi.org/10.1080/18811248.1983.9733476 (1983).
65. Manzel, R. & Walker, C. T. EPMA and SEM of fuel samples from PWR rods with an average burn-up of around 100 MWd/kgHM. *J. Nucl. Mater.* **301**, 170–182 https://doi.org/10.1016/s0022-3115(01)00753-x (2002).
66. Götzmann, O. Thermochemical evaluation of PCI failures in LWR fuel pins. *J. Nucl. Mater.* **107**, 185–195 https://doi.org/10.1016/0022-3115(82)90420-2 (1982).
67. Liu, J. et al. Non-stoichiometric and Subnano-heterogeneous Ln-incorporated UO2: its defect chemistry and thermal oxidation. Preprint at https://doi.org/10.48550/arXiv.2412.03501 (2024).
68. Spino, J. & Peerani, P. Oxygen stoichiometry shift of irradiated LWR-fuels at high burn-ups: Review of data and alternative interpretation of recently published results. *J. Nucl. Mater.* **375**, 8–25 https://doi.org/10.1016/j.jnucmat.2007.10.007 (2008).
69. Vinograd, V. L. & Vauchy, R. A thermodynamic study of fluorite/bixbyite equilibria in the UO_2–$PuO_{1.5}$–PuO_2 system. *J. Nucl. Mater.* **619**, 156244 https://doi.org/10.1016/j.jnucmat.2025.156244 (2026).
70. Tessman, J. R., Kahn, A. H. & Shockley, W. Electronic polarizabilities of ions in crystals. *Phys. Rev.* **92**, 890–895 https://doi.org/10.1103/PhysRev.92.890 (1953).
71. Zhao, R. et al. A facile additive-free method for tunable fabrication of UO_2 and U_3O_8 nanoparticles in aqueous solution. *CrystEngComm* **16**, 2645–2651 https://doi.org/10.1039/c3ce42140f (2014).
72. Tyrpekl, V. et al. Implementation of a spark plasma sintering facility in a hermetic glovebox for compaction of toxic, radiotoxic, and air sensitive materials. *Rev. Sci. Instrum.* **86**. https://doi.org/10.1063/1.4913529 (2015).
73. Carbol, P., Fors, P., Van Winckel, S. & Spahiu, K. Corrosion of irradiated MOX fuel in presence of dissolved H_2. *J. Nucl. Mater.* **392**, 45–54 https://doi.org/10.1016/j.jnucmat.2009.03.044 (2009).
74. Toby, B. H. & Von Dreele, R. B. GSAS-II: the genesis of a modern open-source all purpose crystallography software package. *J. Appl. Crystallogr.* **46**, 544–549 https://doi.org/10.1107/S0021889813003531 (2013).

75. Scheinost, A. C. et al. ROBL-II at ESRF: a synchrotron toolbox for actinide research. *J. Synchrotron Radiat.* **28**, 333–349 https://doi.org/10.1107/S1600577520014265 (2021).
76. Jacobson, N. S., Colle, J. Y., Stolyarova, V., Markus, T. & Nuta, I. Knudsen effusion mass spectrometry: current and future approaches. *Rapid Commun. Mass Spectrom.* **38**, e9744 https://doi.org/10.1002/rcm.9744 (2024).
77. Grønvold, F. High-temperature X-ray study of uranium oxides in the UO_2-U_3O_8 region. *J. Inorg. Nucl. Chem.* **1**, 357–370 https://doi.org/10.1016/0022-1902(55)80046-2 (1955).

Acknowledgements

The experimental data used in this research were partly generated through access to the ActUsLab FMR under the Framework for access to the Joint Research Centre physical Research Infrastructures of the European Commission (Cassius project, Research Infrastructure Access Agreement N° 36618/03). The authors acknowledge the European Synchrotron Radiation Facility (ESRF) for the allocation of beamtime under proposal number CH-7426. The authors acknowledge Herwin Hein and Thomas Gouder for carrying out the supporting measurements, Andrey Bukaemskiy and Victor Vinograd for the productive discussions regarding the microstructure and CsI speciation.

Author contributions

The project was conceived and developed by Daniil Shirokiy and Gabriel L. Murphy. Research methodology, experimental planning and formal analysis were conducted by Daniil Shirokiy, Karin Popa, and Gabriel L. Murphy. Supervision and funding acquisition was performed by Dirk Bosbach, Karin Popa and Gabriel Murphy. Synthesis of materials was done by Karin Popa, Daniil Shirokiy and Marco Cologna. X-ray diffraction was performed by Olaf Walter and Karin Popa. Electron microscopy imaging was performed by Felix Brandt, Martina Klinkenberg, Walter Bonani, Ana Isabel Martinez Ferri and Daniil Shirokiy. X-ray absorption spectroscopy was performed by Damien Prieur. Knudsen effusion mass spectrometry was performed by Jean-Yves Colle, Ondřej Beneš, and Daniil Shirokiy. Inductively coupled plasma mass spectrometry was performed by the in-house Analytical Service at the JRC Karlsruhe led by Răzvan Buda. Manuscript writing, and editing was performed by Daniil Shirokiy and Gabriel L. Murphy with input by all co-authors.

Funding

The authors are grateful to funding and support from the German Federal Ministry of Federal Ministry for Research, Technology and Aeronautics (BMTFR) under funding code 02NUK088A for Project Transient which has supported this research. The authors are grateful to the funding and support from the Helmholtz Graduate School for Energy and Climate Research (HITEC) at Forschungszentrum Juelich GmbH. The authors are also grateful for the funding and support from EURAD 2 working package SAREC grant number ID: 101166718. Open Access funding enabled and organized by Projekt DEAL.

Competing interests

The authors declare no competing interests.

Additional information

Supplementary information The online version contains supplementary material available at https://doi.org/10.1038/s43246-026-01411-7.

Correspondence and requests for materials should be addressed to Daniil Shirokiy, Karin Popa or Gabriel L. Murphy.

Peer review information *Communications Materials* thanks Ericmoore Jossou, Michael Tonks and the other, anonymous, reviewer(s) for their contribution to the peer review of this work. A peer review file is available.

Reprints and permissions information is available at http://www.nature.com/reprints

Publisher's note Springer Nature remains neutral with regard to jurisdictional claims in published maps and institutional affiliations.

Open Access This article is licensed under a Creative Commons Attribution 4.0 International License, which permits use, sharing, adaptation, distribution and reproduction in any medium or format, as long as you give appropriate credit to the original author(s) and the source, provide a link to the Creative Commons licence, and indicate if changes were made. The images or other third party material in this article are included in the article's Creative Commons licence, unless indicated otherwise in a credit line to the material. If material is not included in the article's Creative Commons licence and your intended use is not permitted by statutory regulation or exceeds the permitted use, you will need to obtain permission directly from the copyright holder. To view a copy of this licence, visit http://creativecommons.org/licenses/by/4.0/.

© The Author(s) 2026